Support-induced effect on the catalytic properties of Pd particles in water denitrification: Impact of surface and structural features of mesoporous ceria-zirconia support

Pascal Granger, S. Troncéa, Jean-Philippe Dacquin, Martine Trentesaux, Vasile I. Parvulescu

Revised version submitted to the Journal Applied Catalysis B: Environmental

Manuscript ID : APCATB-D-17-02496

Support-induced effect on the catalytic properties of Pd particles in water denitrification : Impact of surface and structural features of mesoporous ceria-zirconia support

P. Granger, [1*] S. Troncéa,[1,2] J.P. Dacquin,[1*] M. Trentesaux,[1] V.I. Parvulescu,[2*]

[1] Univ. Lille, CNRS, Centrale Lille, ENSCL, Univ. Artois, UMR 8181 - UCCS - Unité de Catalyse et Chimie du Solide, F-59000 Lille, France
[2] University of Bucharest, Department of Organic Chemistry, Biochemistry and Catalysis,B-dul Regina Elisabeta 4-12, Bucharest 030016, Romania.

Corresponding authors :

Prof. Pascal Granger
Email. : pascal.granger@univ-lille1.fr
Phone number : +33 320434938

Dr. Jean-Philippe Dacquin
Email. : jean-philippe.dacquin@univ-lille1.fr
Phone number : +33 320434795

Prof. Vasile I. Parvulescu
Email. : vasile.parvulescu@chimie.unibuc.ro
Phone number : +40 214100241

Abstract

The support effect on the catalytic properties of palladium particles has been investigated in the reduction of nitrites by hydrogen at 20°C in batch conditions. The support material was composed of ceria-zirconia mixed oxide stabilized in the tetragonal structure according to an Evaporation Induced Self-Assembly method. In comparison, a co-precipitation method leads to inhomogeneity in composition related to the partial segregation of the cubic fluorite structure of CeO_2. Further textural properties obtained for the two synthesis routes differ as well as changes in the reducibility. Surface analysis demonstrated a more extensive surface reduction of Ce^{4+} to Ce^{3+} on the series prepared by coprecipitation correlated to a greater stabilization of metallic Pd particles. However, the best catalytic performances were obtained on low loaded Pd samples supported on the ceria-zirconia support prepared by the Evaporation Induced Self-Assembly method which emphasizes the fact that catalytic properties cannot be simply explained by the stabilization of zero valent precious metal at the vicinity of anionic vacancies. Further calculations of TOF and interfacial rates were achieved and compared to the selectivity behavior suggesting that the localization of Pd in contact with the tetragonal or cubic structure of the solid solution and CeO_2 could play a key role in determining the catalytic properties.

Keywords *:* Palladium, mesoporous materials, $Ce_{0.5}Zr_{0.5}O_2$ mixed oxides, Catalytic nitrite reduction, drinking water

1. Introduction

The European Community has set the maximum permitted level of nitrate in drinking water to 50 mg/L because of its adverse health effects [1]. The U.S. Environmental Protection Agency has lowered that level to 10 mg/L [2]. The removal of nitrates from drinking water is not trivial because of the high stability of ionic species and soluble nature. To comply with the legislation, a specific treatment of drinking water is necessary. Up to now, biological and physicochemical treatments allow effective removal of nitrates. On the other hand, they have several economic and ecological disadvantages as reported elsewhere [3]. Catalytic processes are among the most promising technologies and the liquid phase hydrogenation of nitrates to nitrogen by gaseous hydrogen over precious metal based catalysts could represent a valuable alternative [3-5]. In this specific case, some important technical issues were addressed such as the catalyst stability and selectivity in order to lower the production of ammonia as side product. Successful attempts have been already reported combining the advantage of catalysis and ion exchange leading to a complete suppression of ammonium [6]. The shaping of the catalyst, most suited for separating the catalyst of the reaction mixture, is also an important outcome. Recently, Durkin et al. [7] demonstrated that supported Pd-In particles on milled linen fibers are robust and stable exhibiting a stable catalytic activity for nitrate reduction after evaluation during four months. Negligible metal leaching was observed emphasizing an innovative and scalable approach for water purification.

Nitrate reduction can be described by consecutive and parallel reactions where nitrates are first reduced to nitrites in the presence of hydrogen, then ultimately converted to gaseous nitrogen as target product. However, the formation of ammonia as undesired by-product can occur and must be limited with maximum concentration allowable fixed at 0.5 mg/L. [8-11]. The reduction of nitrates to nitrites is usually recognized as structure-insensitive reaction [12]. On the other hand, the sequential reduction of nitrites to N_2 is a structure-sensitive reaction depending on size and morphology of noble metal particles [13]. The complete reduction of nitrates to nitrogen is generally activated on bimetallic particles with high efficiency when palladium is combined with copper [5,13-15]. Up to now, the catalysts used for such an application are mostly characterized by high palladium loading recognized as the most active precious metal [16-18]. One of the

reasons, of such high metal loading could be likely due to a strong deactivation because of particle sintering in aqueous phase and loss of metallic character of palladium particles. Local variations of the concentration of OH^-, produced during the reaction, inside the porous structure of the host matrix could also favor the adsorption of hydroxyl groups over precious metals inducing a strong inhibition of the reaction rate. A side effect is also related to an alteration of the selectivity becoming more favorable toward ammonia formation. Hence, open mesoporous network could facilitate mass transfer phenomena then minimizing gradient concentrations and related detrimental effects on the catalytic activity and selectivity. Some attempts were also reported by substituting conventional alumina or silica supports by carbon based supports but, unfortunately, those systems were found more selective toward ammonia formation [16]. Further improvements were reported on reducible TiO_2 support [19]: The creation of strong-metal support interactions stabilize more active electron-rich active metal state via the formation of partially reduced TiO_{2-x} aggregates. A careful monitoring of the electron density, as reported elsewhere on Pt/CeO_2, could be of great importance to prevent over hydrogenation process leading inevitably to the production of ammonia [20]. A strengthening of the metallic character could prevent corrosion by water and particle aggregation phenomena.

This study reports the behavior of supported palladium catalysts on ceria-zirconia support. CeO_2-ZrO_2 mixed oxides in a mesoporous structure containing crystalline walls are expected to provide enhanced catalytic performances due to their large surface area and a certain degree of size and shape selectivity. Sanchez et al. reported the first successful fabrication of cubic mesostructured CeO_2-ZrO_2 thin films [21]. It is possible to adjust the textural properties of CeO_2-ZrO_2 mixed oxides by utilizing different methods of preparation. Accordingly, a soft templating method such as evaporation induced self-assembly (EISA) as novel direct method for preparing mesoporous $Ce_{0.5}Zr_{0.5}O_2$ with controlled porosity is compared to more conventional co-precipitation methods. The catalytic reduction of nitrites to nitrogen have been investigated on monometallic $Pd/Ce_{0.5}Zr_{0.5}O_2$ with regard to the impact of the mesostructure as well as the extent of the Pd-support interaction, modulated by the pre-activation thermal treatment, on the catalytic activity and selectivity. Interestingly, it was found that the prerequisites for developing the catalytic performances could differ according to the reducibility of the support materials compared to conventional supported silica or alumina systems as well as on the preparation method.

2. Experimental

2.1. Catalyst preparation

2.1.1. $Ce_{0.5}Zr_{0.5}O_2$ support materials

$Ce_{0.5}Zr_{0.5}O_2$ was prepared according to two different experimental protocols. The EISA method was based on a sol-gel process combined with evaporation-induced self-assembly process in ethanol using block copolymer Pluronic P123 as template and cerium nitrate and zirconium oxychloride as precursor salts [22]. 0.5 g of Pluronic P123 (supplied by Aldrich) was dissolved in 10 mL of ethanol. Then the solution obtained after dissolution in ethanol of $Ce(NO_3)_3.6H_2O$ and $ZrOCl_2 \cdot 8H_2O$ (supplied by Sigma Aldrich) precursor salts was added. After stirring for 3 hours at room temperature, the homogeneous solution was transferred to an oven under desired temperature and humidity (temperature 40°C, and relative humidity: 50%) and underwent solvent evaporation. After 48 hours aging, the gel product was dried first at 60°C for 24 hours and then at 100°C for another 24 hours, in order to favor the interaction between the precursors and the polymer which originated the mesoporous structure [22].

For the co-precipitation method (COP), $Ce(NO_3)_3.6H_2O$ and $ZrOCl_2 \cdot 8H_2O$ were dissolved in distilled water under magnetic stirring and then heated at 60°C. Cerium and zirconium hydroxides were precipitated by adding dropwise ammonia solution up to pH = 10 and the suspension was stirred for 4 hours. The solid precursor was washed with distilled water several times before aging at room temperature for 48 hours, and drying at 120°C for 24 hours [23].

The solid oxy-hydroxide precursors obtained through these two methods were calcined in air at 400°C for 4 hours. The temperature gradually increased with a gradient temperature of 1°C/min.

2.1.2. Impregnated $Pd/Ce_{0.5}Zr_{0.5}O_2$ catalysts

The monometallic catalysts were prepared by incipient wetness impregnation from aqueous solutions of palladium nitrates ($Pd(NO_3)_2 \cdot 2H_2O$, Sigma Aldrich) with concentration adjusted to get 2.3 wt.% or 0.46 wt.% Pd [24]. After impregnation, the precursors were dried in air at 105°C overnight, calcined in air at 400°C for 2 hours and finally reduced in pure hydrogen at 300°C or 500°C for 4 hours with a heating rate of 5°C/min and a H_2 flow of 60 $mL.min^{-1}$. The reduced

catalysts were finally labeled xPd/CZ(EISA) and xPd/CZ(COP) where x stands for the weight palladium loading equal to 0.46 or 2.3 wt.%.

2.2. Physicochemical characterization

2.2.1. Bulk characterization

Thermogravimetric analyses (TGA) were carried out on a TA Instrument DSC-TGA SDT 2960 thermal analyzer in the temperature range of 25-900°C under air. The heating rate was kept constant to 10°C/min.

X-ray diffraction (XRD) patterns were recorded on a HUBER G-670 diffractometer fitted with an anti-cathode CuKα (λ = 1.54178 Å). XRD patterns were recorded over 2θ values ranging from 10° to 80°, with a scanning rate of 5s/step and 0.05 step sizes. Low-angle XRD patterns were recorded on a D8 advances X-ray diffractometer (Bruker AXS) fitted with a CuKα (λ = 1.54178 Å) radiation in the 2θ range 0.3-6° with a 0.02° steps.

Raman spectra were recorded in a Labram Infinity Dilor spectrometer equipped with a frequency-doubled Nd:YAG laser corresponding to an excitation radiation of 532 nm. The silicon line at 521 cm^{-1} was used for calibration. The exciting wavelength from an Ar ion laser with a power of 4 mW on the samples was 514.5 nm. The scanning range was set between 100 and 1800 cm^{-1}.

The bulk redox properties were investigated from H_2-Temperature-Programmed Reduction experiments (H_2-TPR) on a Micromeritics Autochem II 2920 under a flow of 5 vol.% H_2 in Ar and a gradual heating rate of 5°C/min. Scanning Emission Microscopy images were recorded on a Hitachi SU-70, SEM-FEG microscope.

The elemental analysis was performed by inductively coupled plasma-optic emission spectroscopy 720-ES ICP-OES (Agilent) with axially viewing and simultaneous CCD detection. The ICP Expert™ software (version 2.0.4) provided the concentration of metal in sample allowing estimating the weight percentage of Pd.

2.2.2. Surface characterization

The textural properties were analyzed from nitrogen adsorption-desorption experiments at -196°C using a Micrometrics Tristar 3020 apparatus. Prior to adsorption, all samples were systematically degassed at 200°C under vacuum for 4 hours. The specific surface area was calculated from the BET equation and the pore volume (V_p) was estimated using the adsorption branch of the nitrogen isotherm curve at $P/P_0 = 0.98$ single point.

XPS experiments were performed under ultra-high vacuum (UHV) (~10^{-10} Torr) using a Vacuum Generators Escalab 220XL spectrometer equipped with a monochromatized aluminum source for excitation. Binding energy (B.E.) values were referenced to the binding energy of the C 1s core level at 285.1 eV. The relative quantification was achieved using a mixed Gaussian /Lorentzian peak fit keeping binding energies and half-width constant for all spectral decompositions.

Palladium dispersion was calculated from H_2 chemisorption measurements performed on a Micromeritics Autochem II 2920 apparatus. Prior to chemisorption, all samples were pre-reduced at 300°C or 500°C under a flow of 20 mL/min of pure hydrogen and outgassed at the selected temperature in argon. H_2 pulses with 5 vol.% H_2 in Ar where injected until saturation at 100°C to avoid overestimation of H_2 uptake due to palladium hydride formation [25]. The dispersion was calculated according to the stoichiometric ratio H/Pd = 1.

2.3. Catalytic measurements

The nitrite reduction reaction was performed in a 250 mL batch reactor equipped with a magnetic stirrer operating at atmospheric pressure. 80 or 400 mg of catalyst in powder form, with average grain size of 250 μm, were introduced in the reactor and then purged with pure H_2 for 1 hour at RT. In the second stage, 40 mL of ultrapure water was add to the system under a flow of H_2 (200 mL/min) for 1 hour. Afterwards, 10 mL of nitrites solution (500 mg/L or 100 mg/L) were introduced and the suspension was stirred with a the rotation speed set at 700 rpm. The experiment was carried out at 20°C with a H_2 flow rate of 200 mL/min. Nitrite concentration was monitored by an ionic chromatograph (Metrohm 844 UV/VIS Compact IC–Column Metrosep A Supp 16-250/4.0). The concentration of ammonium ions were measured by using an ion chromatograph (Metrohm 861 Advanced Compact IC – column Metrosep C 6 -250/4.0).

3. Results and discussion

3.1. Influence of the synthesis route of $Ce_{0.5}Zr_{0.5}O_2$ on the physicochemical properties: Structural vs. textural properties

3.1.1. Thermal decomposition of solid precursors of Ce-Zr mixed oxides prepared by coprecipitation and EISA

TG-DSC curves vs. temperature performed on the solid precursors of $Ce_{0.5}Zr_{0.5}O_2$ prepared via the EISA and the coprecipitation methods are reported in Figs. 1(a) and 2 respectively. To complement those observations, the TG and heat flow curves vs. temperature curves recorded on the precursors of the single oxides (CeO_2 and ZrO_2) are recorded in Fig. S1 in Supplementary Materials. The weight loss profile recorded on the EISA precursor is similar to that previously reported on $Ce_xZr_{1-x}O_2$ according to the same preparation method [26]. Below 150°C, the endothermic water evaporation takes place. The strong discontinuity, appearing in the weight profile at 180°C, can be ascribed to the combustion of the copolymer template (pluronic 123) and could be catalyzed by the presence of cerium as discussed in Supplementary Materials.

The identification of processes occurring at 290°C and 350°C is somewhat easier by comparing with *in situ* Raman spectroscopic measurements in Fig. 1(b) on the precursor exposed to O_2/He mixture. As seen, three broad Raman lines appear distinctly from 320°C centered at 300 cm^{-1}, 490 cm^{-1} and 620 cm^{-1}. The Raman line at 490 cm^{-1} is characteristic of the F_{2g} mode of the cubic fluorite-like structure [27-30]. This value is higher than that of the peak in the spectrum of pure CeO_2, as a result of reducing cell parameters due to the insertion of the Zr^{4+} ion with a smaller radius than Ce^{4+} (0.84 Å vs. 0.97 Å) [31]. The band at 620 cm^{-1} can be attributed to a non-degenerate longitudinal optical (LO) mode of ceria induced by the oxygen vacancies in the ceria lattice [32-34]. The bands near 300 cm^{-1} could be tentatively related to the displacement of oxygen atoms from their ideal fluorite lattice positions by the zirconium insertion into the CeO_2 lattice with the formation of the pseudo-cubic (*t"*) phase [10,35]. Hence, based on those observations and related assignments, a predominant growth of a cubic structure would start at rather low temperature emphasizing a predominant formation of solid solution in rather good agreement with the absence of significant signal above 450°C ascribed to the crystallization of the metastable tetragonal structure of ZrO_2 (see Fig. S1(d)). Let us note that, in this domain of

composition, the stabilization of a tetragonal structure for the $Ce_{0.5}Zr_{0.5}O_2$ solid solution cannot be completely ruled out. TG analysis on the precursor obtained by coprecipitation (Fig. 2) also evidences processes occurring more smoothly in the absence of surfactant.

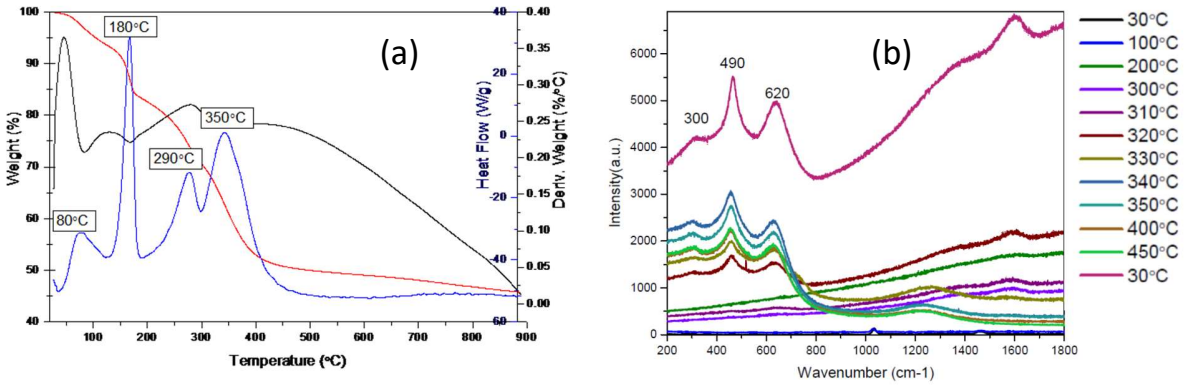

Fig. 1. (a) TG-DSC analysis with weight loss profile in red, the derivative weight curve in blue and the heat flow profile in black and (b) *in situ* Raman spectroscopic measurements performed on the precursor of $Ce_{0.5}Zr_{0.5}O_2$ prepared according to the EISA procedure – *In situ* Raman spectroscopic measurements were performed under a flow of oxygen diluted in He (O_2/He = 1.7) with a heating rate dT/dt = 5°C/min.

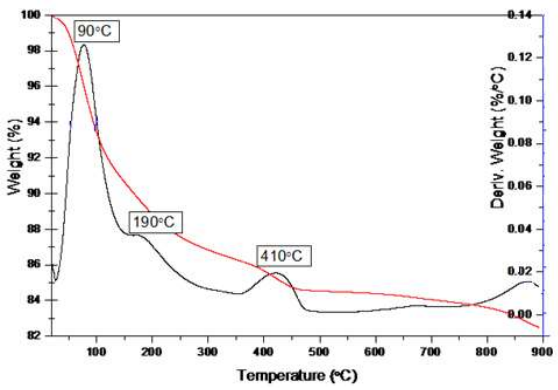

Fig. 2. TG analysis performed on the precursor of $Ce_{0.5}Zr_{0.5}O_2$ prepared according to the coprecipitation method.

3.1.2. Structural properties of $Ce_{0.5}Zr_{0.5}O_2$ mixed oxides calcined at 400°C

Wide angles X-ray Diffraction analysis

X-ray diffraction pattern on CeO_2 in Fig. 3(a) is characterized by reflections (111), (200), (220) and (311) at 2θ values of 28.5°, 33.0°, 47.4°, 56.2°, corresponding to the cubic structure of CeO_2 (JCPDS 34-0394). For ZrO_2, the main reflections at 2θ values of 30.2°, 35.3°, 50.2°, 60.1° are

characteristic of a tetragonal structure (JCPDS 81-15). In most cases, changes observed in the structural features of the fluorite lattice of CeO_2 are highlighted by discernible shifts on the 2θ values when cerium is partially substituted by zirconium. This could be attributed to deformations inducing some modifications of the interplanar spacing when Ce^{4+} (0.97 Å) is substituted by Zr^{4+} (0.87 Å) having a smaller ionic radius [31,33]. Hence, the 2θ values for $Ce_{0.5}Zr_{0.5}O_2$ at 29.3° and 33.8° are in good agreement with previous observations [36] and consistent with the aforementioned statements. In practice, both the position and peak broadening observed in Fig. 3(a) cannot lead to unequivocal assignments [36,37]. Indeed, for intermediate compositions, the phase diagram of $Ce_xZr_{1-x}O_2$ suggests the coexistence of stable and metastable tetragonal phase and a predominant cubic phase. An interesting observation is related to the lower 2θ values observed on the X-ray pattern of $Ce_xZr_{1-x}O_2$ prepared by co-precipitation (see Fig. 3(b)). According to the aforementioned explanation, this could reflect a weaker insertion of zirconium inside the ceria lattice.

The crystallite sizes have been estimated from the Williamson-Hall method leading to comparable values listed in Table 1.

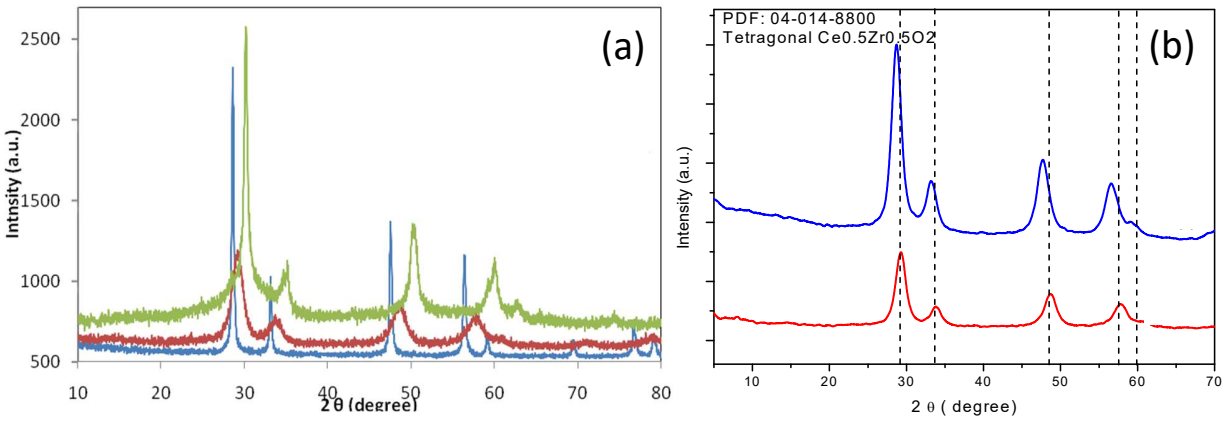

Fig. 3. Wide angles X-ray Diffraction patterns recorded on (a) single oxides reference and mixed $Ce_{0.5}Zr_{0.5}O_2$ after calcination in air at 400°C – CeO_2(EISA) in blue, ZrO_2(EISA) in green and CZ(EISA) in red. (b) X-ray Diffraction patterns of $Ce_{0.5}Zr_{0.5}O_2$ prepared by coprecipitation (blue) and Evaporation Self-Assembly method (red).

Raman spectroscopy

The Raman spectra of CZ(EISA) and CZ(COP) calcined at 400°C are shown in Fig. 4. Raman spectroscopic measurements can complement XRD data since this technique is also sensitive to

amorphous structures. Typically, 6 Raman active modes (A1g + 2B1g + 3E2g) are expected in the case of tetragonal structure characterized by a $P4_2/nmc$ space group instead of one for the F2g mode for a cubic fluorite structure with a space group Fm3m corresponding to an intense Raman line at 490 cm^{-1} in Fig. 4. As reported elsewhere, a significant shift to higher wavenumbers is observed compared to current values earlier reported on pure CeO_2 (465 cm^{-1}) [37]. Additional weaker Raman lines located at 155, 200, 300 and 620 cm^{-1} are discernible on both samples. For CZ(EISA) a broadening of the peak from 490 cm^{-1} can be observed with shoulder at about 550 nm^{-1} which is attributed to the tetragonal (*t*) phase [27]. The bands near 300 cm^{-1} and 180 cm^{-1} for CZ(COP) and CZ(EISA) are related to the displacement of oxygen atoms from their ideal fluorite lattice positions by the zirconium insertion into the CeO_2 lattice with the formation of the pseudo-cubic (*t"*) phase [10,35]. The presence of the band at about 155 cm^{-1} is related to the *t*-ZrO_2 phase [27]. Moreover, all the bands exhibited by COP are red-shifted compared with EISA indicating a lower insertion of ZrO_2 in the CeO_2 lattice. This seems to be consistent with a sharp broadening of the 490 cm^{-1} caused by crystallites size and increasing concentration of crystal defects essentially oxygen vacancies [38]. This explanation is in relative good agreement with a more distinct observation of the 620 cm^{-1} Raman line on the EISA sample previously assigned to a non-degenerate Raman inactive longitudinal of CeO_2 reflecting disturbances of the local M-O bond chemistry leading to the relaxation of its symmetry [32-34]. This band, previously observed on $Ce_xZr_{1-x}O_2$ characterized by a larger amount of defective sites, could suggest some improvement on the bulk redox properties of this materials [39].

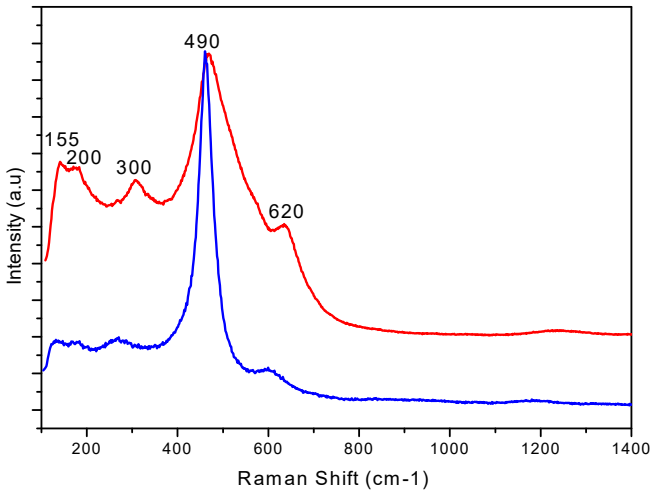

Fig. 4. Raman spectra recorded on $Ce_{0.5}Zr_{0.5}O_2$ prepared by EISA and coprecipitation and calcined at 400°C in air : CZ(COP) in blue and CZ(EISA) in red.

3.1.3. Textural properties of $Ce_{0.5}Zr_{0.5}O_2$ mixed oxides calcined at 400°C

Pore ordering quality of the materials was assessed by low angles XRD (see Fig. 5). As illustrated, a well-defined reflection centered at 0.55° is observed on the dried CZ sample prepared following EISA protocol. This result evidences the genesis of an ordered mesophase (*P6mm* hexagonal symmetry) with respect to the conventional precipitation route. However, the calcination step was partially detrimental for this sample as observed by the broadening and shifting of the X-ray line toward higher 2Θ angle (1.15°). Partial shrinkage of the mesostructure would indubitably occur during the decomposition of the surfactant in the presence of inorganic species. Interestingly, the CZ sample prepared by the coprecipitation route exhibits a broad X-ray line following the calcination step that would probably originate from the loose aggregation of particles at the nanoscale. Hence, mesopores formation can be obtained following these two synthesis routes but arise from different processes.

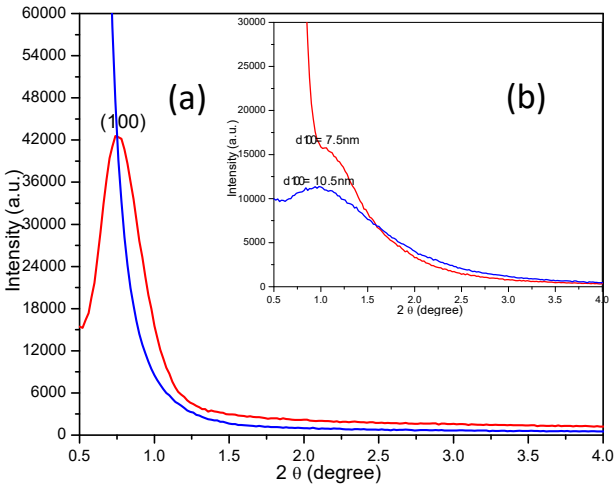

Fig. 5. Low angles XRD diagrams performed on dried samples (a) and calcined samples (insight) (b) – COP in blue and EISA in red.

Further information are given from nitrogen physisorption measurements performed on CZ(EISA) and CZ(COP), as reported in Fig. 6. Both are showing adsorption-desorption profiles of type IV characteristic of mesoporous systems [40]. As observed, the large hysteresis obtained for CZ(COP) would more reflect the presence of agglomerated particle solids as evidenced earlier by low angle XRD. On the other hand, the form of the hysteresis of type H2 for CZ(EISA) would characterize the presence of partially uniform mesopores. The specific surface area, pore volume and average pore size, calculated by the BET and BJH methods (see Table 1) are comparable. On the other hand, narrow pore size distribution obtained on CZ(EISA) in the

range 2-6 nm drastically differ from that obtained on CZ(COP) exhibiting a broader and bimodal distribution in the range 2-12 nm. Similar differences were also previously reported by comparing mesoporous Ce-Zr solid solutions prepared with and without template [41] from respectively the self-assembly of the pluronic template and disordered accumulation in the absence of template. Such differences correctly match the observations from Scanning Electron Microscopy micrographs in Fig. 7 with a sharp pore size distribution discernible for CZ(EIZA). As a matter of fact, comparing the textural features obtained on single oxide, especially the average pore size determined on CeO_2, one could suggest that the presence of inhomogenities could be also the results of heterogeneity in composition with a partial segregation of CeO_2 in the particular case of CZ(COP) in agreement with XRD and Raman spectroscopic measurements.

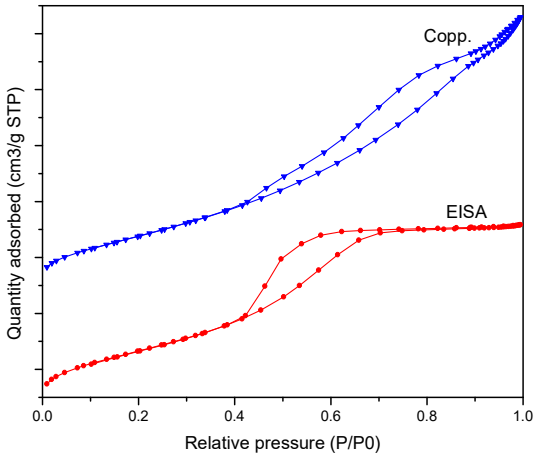

Fig. 6. Nitrogen physisorption isotherms recorded at-196°C on $Ce_{0.5}Zr_{0.5}O_2$ calcined at 400°C – CZ(COP) in blue and CZ(EISA) in red.

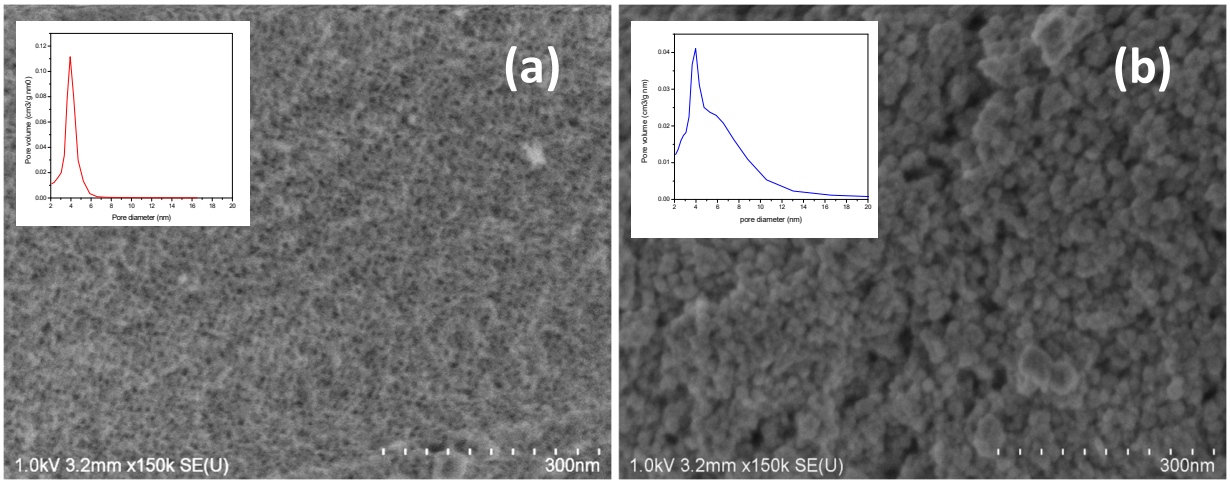

Fig. 7. Scanning Electron Microscopy images recorded on $Ce_{0.5}Zr_{0.5}O_2$ calcined 400°C – CZ(EISA) (a) and CZ(COP) (b).

Table 1. Elemental and textural analysis of $Ce_{0.5}Zr_{0.5}O_2$ prepared by coprecicipation and the EISA method.

Sample	Ce (at.%)	Zr (at.%)	Specific surf. Area ($m^2.g^{-1}$)	Total pore vol. ($cm^3.\ g^{-1}$)	Average pore size (nm)	Crystallite size (nm)
CZ(EISA)	0.35	0.65	98	0.10	4.5	5.6
CZ(COP)	0.43	0.57	100	0.10	6.5	5.2
Ce(EISA)			14	0.04	11.9	
Ce(COP)			52	0.12	9.3	
Zr(EISA)			62	0.10	6.7	
Zr(COP)			132	0.17	5.3	

3.2. Reducibility of bare $Ce_{0.5}Zr_{0.5}O_2$ and doped with palladium

Preliminary observations from H_2-TPR experiments on CeO_2 in Fig. S2 (Supplementary Information) reveal two distinct reduction processes in the temperature range 420-510°C and above 800°C previously ascribed to surface and bulk reduction processes of Ce^{4+} to Ce^{3+} [36,37]. Fig 8(a) shows the H_2 uptake profiles vs. temperature recorded during H_2-TPR experiments on CZ(EISA) and CZ(COP) calcined at 400°C which slightly differs. As observed, an unique broad and intense asymmetric signal is observed on CZ(EISA) with a maximum at ~575°C (peak labeled γ) with a weakly discernible shoulder near 450°C. Similar observations were previously reported showing, in most cases, a broad signal developing below 700°C and tentatively explained by an improvement of oxygen ion mobility induced by the insertion of zirconium inside the ceria lattice [37,42-44]. Interestingly, the shoulder coexisting with peak γ on CZ(COP) intensifies shifting to lower temperature. In addition, an extra reduction process appears, with a maximum around 800°C, previously evidenced during the reduction of pure ceria and suggesting a partial segregation of CeO_2 on this sample coexisting with the tetragonal Ce-Zr solid solution [36].

Subsequent incorporation of palladium drastically improves the reduction of $Ce_{0.5}Zr_{0.5}O_2$ with a sharp shift of peak β to lower temperature. Let us note that the calculated H_2 uptakes of 1.3×10^{-3} and 1.8×10^{-3} mol/g, respectively on 2.3Pd/CZ(EISA) and 2.3Pd/CZ(COP), largely exceed the theoretical H_2 consumption for the bulk reduction of PdO to Pd^0 corresponding to 0.2×10^{-3} mol/g. Particular attention was paid to the additional low temperature reduction process taking place below 150°C corresponding to the reduction of oxidic palladium species. The reduction of PdO to metallic Pd particles was previously observed in the temperature range 60-90°C on

Pd/Ce-Zr-O systems [33,45]. As a matter of fact, the reduction temperature of PdO particles can be both closely related to the nature of support materials, with which they interact, and the particle size. Indeed, numerous investigations found that well-dispersed PdO reduces above 100°C whereas the reduction of larger PdO particles would occur for T≤ 50°C [46-48]. Hence, the absence of signal below 50°C on Pd/CZ(EISA) and Pd(COP) could suggest a strong interaction between PdO and $Ce_{0.5}Zr_{0.5}O_2$ assuming a reduction of PdO partly hindered by the reduction of $Ce_{0.5}Zr_{0.5}O_2$ at least on Pd/CZ(EISA). As a consequence, the appearance of the slight contribution (peak α) on Pd/CZ(COP) could suggest a higher reducibility of PdO partly ascribed to the segregation of larger particles or to the existence of different types of interactions since Fig. 8(a) clearly showed the segregation of Ce-Zr mixed oxide with CeO_2.

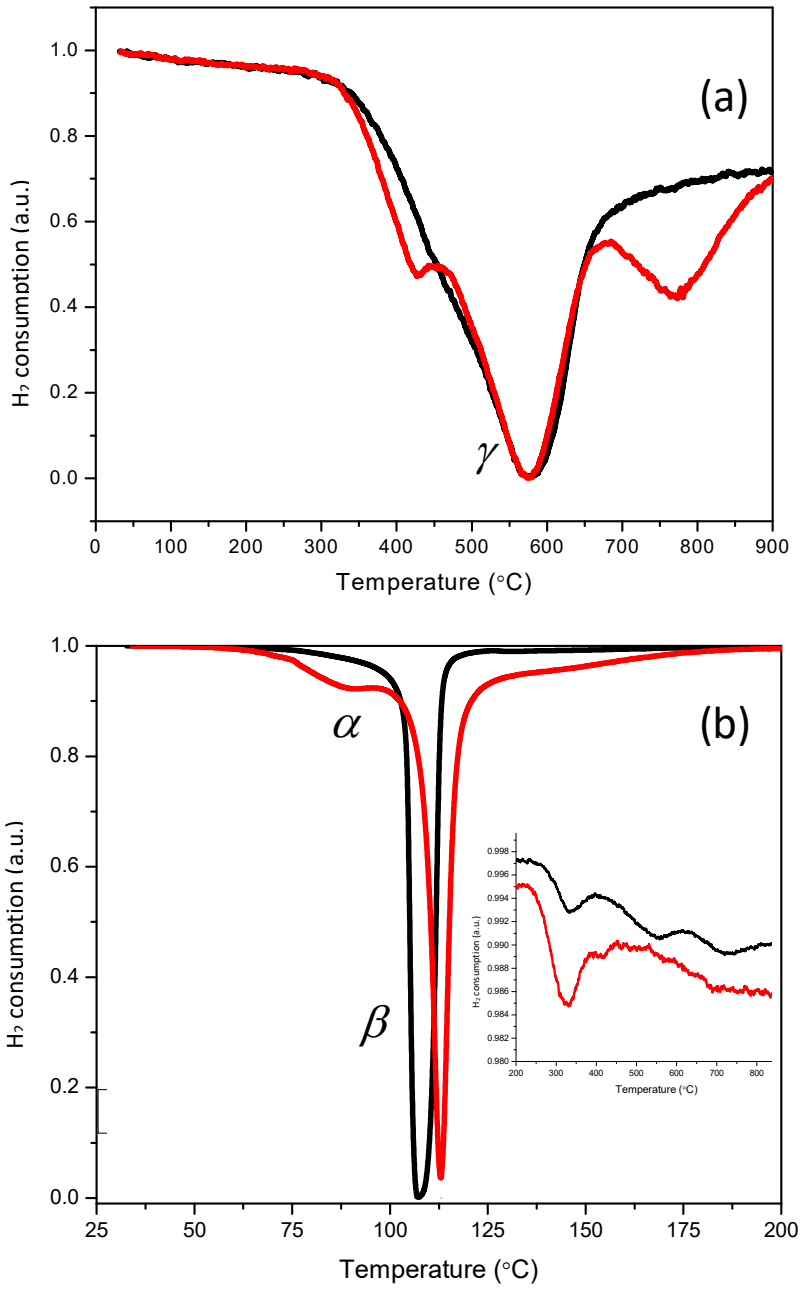

Fig. 8. H_2-TPR experiments performed on bare $Ce_{0.5}Zr_{0.5}O_2$ (a) and Pd-doped $Ce_{0.5}Zr_{0.5}O_2$ (b) – In red CZ(EISA) and Pd/ CZ(EISA) and in black CZ(COP) and Pd/CZ(COP).

3.3. Surface properties

Pd dispersion was estimated from H_2 titration. Chemisorption measurements were performed at 100°C in order to avoid an overestimation on H_2 uptakes due to the current formation of bulk palladium hydrides. As mentioned, a dissociative adsorption with H/Pd =1 has been taken into account leading to the results collected in Table 2. The mean particle size has been roughly calculated assuming hemispherical metallic palladium particles. To check the validity of those calculations the mean Pd particle size of Pd particle on 2.3Pd/CZ(EISA) was measured from TEM analysis leading to a good consistency (7 nm vs. 8.6 nm from H_2 chemisorption). This comparison also underlines the occurrence of weak spill-over effect previously underlined on Rh supported on ceria [44]. As explained, the presence of zirconia and the relative low dispersion on Pd/CZ, could partly explain this observation. As seen, higher Pd dispersion are systematically obtained on the series Pd/CZ(EISA) from direct comparison with their homologues prepared by co-precipitation.

To complement these measurements, *ex situ* XPS measurements were performed on calcined samples and reduced in H_2 at 400°C. Let us note that reduced samples were stored in ambient atmosphere prior to XPS analysis. The characteristic Zr 3d, Ce 3d, O1s and Pd 3d core levels were analyzed. The Binding Energy (B.E.) values obtained from the photopeak Zr $3d_{5/2}$ in the B.E. range 182.4-183.5 eV essentially evidence the presence of Zr^{3+} species. More complex spectral features usually characterize the Ce 3d photopeak which can be decomposed into different components u, u', u'', u''' and v, v', v'', v''' as illustrated in Fig. 9 [49]. In this particular case, the predominance of Ce^{3+} or Ce^{4+} can be determined from the integration of the peak area relative to these different components leading to the estimation of the Ce^{3+}/Ce^{4+} ratio in Table 2. Regarding the analysis of the Pd 3d photopeak, some disturbances arose due to overlappings with the Zr 3p photopeak then lowering the accuracy on the quantitative analysis,

especially for low loaded samples. Let us note that the B.E. values for the Pd $3d_{5/2}$ core level essentially characterize the presence of oxidic palladium species indicating a significant reoxidation of *ex situ* reduced samples. However, an additional contribution can be isolated on the Pd/CZ(COP) at 335.5-335.7 eV which could reflect the presence of Pd^0 [50,51] and/or Pd_xO clusters [52]. Let us note that in all cases the B.E. values diverge than those currently reported for PdO in the range 336.1-336.9 eV [53]. The contribution appearing in the range 337.4-338.4 eV could correspond to the stabilization of Pd^{4+}, possibly stabilized as PdO_2, as reported elsewhere [53-55] and/or the formation of PdO_y with $1 < y < 2$ caused by the diffusion of oxygen in PdO [52]. As a matter of fact, the observation of high B.E. can have different origins reflecting electron transfer processes governed by the extent of interaction with the support and/or the influence of particle size then stabilizing electron deficient $Pd^{\delta+}$ species with $\delta > 2$.

Semi-quantitative analysis provides important information revealing significant divergences on the relative cerium composition at the surface. As indicated in Table 2, bare and doped ceria-zirconia supports prepared by the EISA method exhibit a zirconium surface enrichment whereas cerium enrichment is systematically observed on the series prepared by co-precipitation consistent with a partial segregation of CeO_2. Regarding the palladium concentration, no significant deviation is observed after *ex situ* reduction which could suggest particle sintering. On the other hand, the calculation of the Ce^{3+}/Ce^{4+} ratio led to significant evolutions on the reduced Pd/CZ(COP) samples with a sharp increase which could reflect a greater reducibility of surface Ce^{4+} stabilized as CeO_2 instead of $Ce_xZr_{1-x}O_2$ solution.

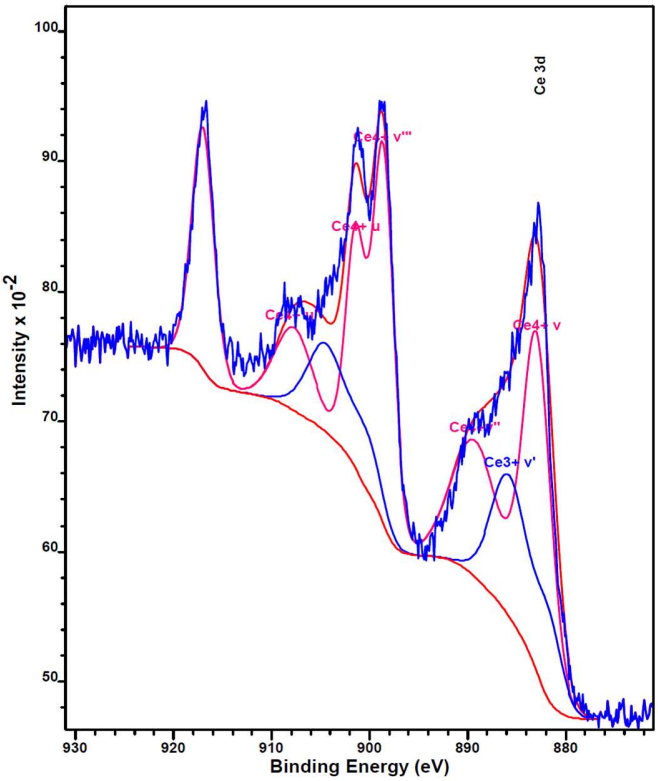

Fig. 9. Typical example of the decomposition of the Ce 3d photopeak recorded on 0.46Pd/CZ(EISA).

Table 2. XPS analysis of Pd-doped $Ce_{0.5}Zr_{0.5}O_2$ – Influence of the reduction temperature on the composition and oxidation state of elements.

Catalyst	Thermal Pretreatment	Pd Disp.[a] (%)	Mean Particle size[b] (nm)	B.E. (eV) Zr $3d_{5/2}$	Ce $3d_{5/2}$	O 1s	Pd $3d_{5/2}$	Relative surface composition Zr/Ce	Pd/Ce+Zr	O/Ce+Zr	Ce^{3+}/Ce^{4+}
CZ(EISA)	none	-	-	183.5	883.9	530.9	-	1.21	-	2.25	0.57
CZ(COP)	none	-	-	182.8	883.7	530.5	-	0.45	-	2.50	0.52
0.46Pd / CZ(EISA)	none			182.5	882.9	530.1	338.1	1.80	0.70×10^{-2}	2.20	0.42
0.46Pd / CZ(EISA)	H_2/300°C [c]	13.0	8.6	182.3	882.6	529.9	337.9	1.71	0.83×10^{-2}	1.97	0.64
2.3Pd / CZ(EISA)	none			183.0	883.7	530.4	338.4	1.37	5.66×10^{-2}	2.34	0.29
2.3Pd / CZ(EISA)	H_2/300°C [c]	18.2	6.1	183.0	883.1	530.5	338.5	1.42	3.39×10^{-2}	2.05	0.32
0.46Pd / CZ(COP)	none			182.6	882.7	530.1	337.8	0.84	6.18×10^{-2}	2.81	0.21
0.46Pd / CZ(COP)	H_2/300°C [c]	5.8	19.2	182.3	882.7	529.9	338.4/335.7	0.75	6.97×10^{-2}	3.04	1.19
2.3Pd / CZ(COP)	none			182.5	883.1	530.4	337.3	0.93	-	2.69	0.35
2.3Pd / CZ(COP)	H_2/300°C [c]	10.3	10.9	182.4	883.1	530.0	338.0/335.5	1.00	5.41×10^{-2}	1.29	1.20

[a] from H_2 titration at 100°C on pre-reduced samples in pure H_2 at 300°C

[b] calculated from the palladium dispersion

[c] *ex situ* reduced in pure H_2 then stored in air at room temperature (XPS analysis were performed on sample stored in air)

3.4. Catalytic properties of $Pd/Ce_{0.5}Zr_{0.5}O_2$ in the reduction of nitrite by hydrogen

3.4.1. Estimation of initial rates

Fig. 10 illustrates the conversion of nitrites, $X(NO_2^-)$ and the concentration of ammonium ions profiles vs. time in a stirred tank reactor. Ammonia formed by extensive reduction of nitrites is stabilized as ammonium ions in the reaction media. The influence of Pd loading and pre-reduction temperature on the rate of nitrites conversion and ammonia formation was examined. Let us keep in mind that catalytic measurements were performed in batch conditions with the same amount of palladium by introducing inside the reactor 80 or 400 mg of respectively 2.3 wt.% and 0.46 wt.% Pd/CZ corresponding to a total number of 6.5×10^{19} Pd atoms. The normalized initial specific rates expressed per gram of palladium were calculated from the slope of the tangent in t = 0 leading to the rate values collected in Table 3. As shown, these values calculated on reduced sample at 300°C are sensitive to the preparation method and the palladium loading. In these operating conditions, the superiority of 0.46Pd/CZ(EISA) is clearly demonstrated from the comparison of the normalized specific rates. Let us note that this tendency is also conserved when the catalysts were pre-reduced at higher temperature, i.e., 500°C, prior to reaction.

Further comparisons of normalized rates and TOF estimates from previous investigations are not so evident because in most cases, kinetic studies were performed at 25°C while we selected a lower temperature, i.e., 20°C [56-58]. Anyway, it is worthwhile to note that the TOF values on 0.46Pd/CZ(EISA) is one order of magnitude higher compared to that measured on highly loaded 6.24 wt.% Pd supported on alumina [56]. By comparing the normalized rate expressed per gram on 4.67 wt.% Pd dispersed on pillared clays, 0.46Pd/CZ(EISA) still demonstrates its superiority (14.2 vs. 263 $mmol.min^{-1}.g_{Pd}^{-1}$) [57]. Chinthaginjala and Lefferts [58] reported relevant steady-state kinetic data measured in a fixed bed flow reactor which account for the occurrence of deactivation effects. In their operating conditions at 25°C, the TOF is two order of magnitude lower than that calculated on 0.46Pd/CZ(EISA). Despite different reactor design (batch vs. continuous flow reactor), this latter comparison suggests that 0.46Pd/CZ(EISA) could be potentially a good candidate for further practical developments.

3.4.2. Selectivity towards the formation of ammonium ions

Significant information is also related to the selectivity behavior of Pd/CZ samples with the formation of undesired products such as ammonia. As exemplified in Fig. S3, an important rise in ammonia concentration occurs at the initial stage of the reaction and then stabilizing on Pd/ZrO_2 as reported elsewhere on different catalytic systems [59-61]. As shown in Fig. 11, Pd/CZ behaves differently mimicking the selectivity recorded on Pd/CeO_2 with a volcano type curve suggesting the occurrence of sequential processes involving the formation and the consumption of ammonia (see Figs. S3(b) and 11). The literature reporting such a behavior is scarce [62,63]. Additional information relative to the involvement of sequential processes can be obtained : – (i) Ammonium ions concentration gradually decreases while nitrites are completely converted as exemplified on 0.46Pd/CZ(EISA) which could rule out an hypothetical direct redox reaction between NH_4^+ and NO_2^- contrarily to previous assumptions [63]. – (ii) Qualitatively, the sequential consumption of ammonium ions seems to occur more readily on sample reduced at 500°C by comparing the ammonium concentration at the maximum and at the end after 6 hours reaction. As exemplified, this sequential reaction process does not occur significantly on 0.46Pd/CZ(COP) reduced at 300°C.

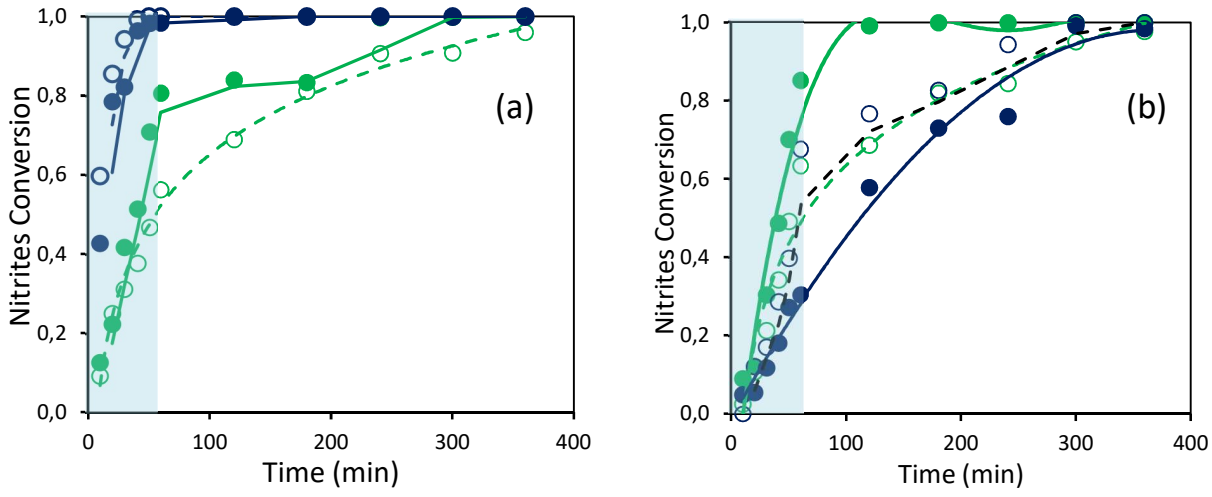

Fig. 10. Influence of the palladium loading and reduction temperature on the conversion profiles vs. time during the reduction of nitrites by hydrogen in batch conditions : (a) on Pd/CZ(EISA) and (b) Pd/CZ(COP) – full symbol reduction at 300°C, open symbol reduction at 500°C – 0.46 wt%Pd in blue and 2.3 wt.% Pd in green.

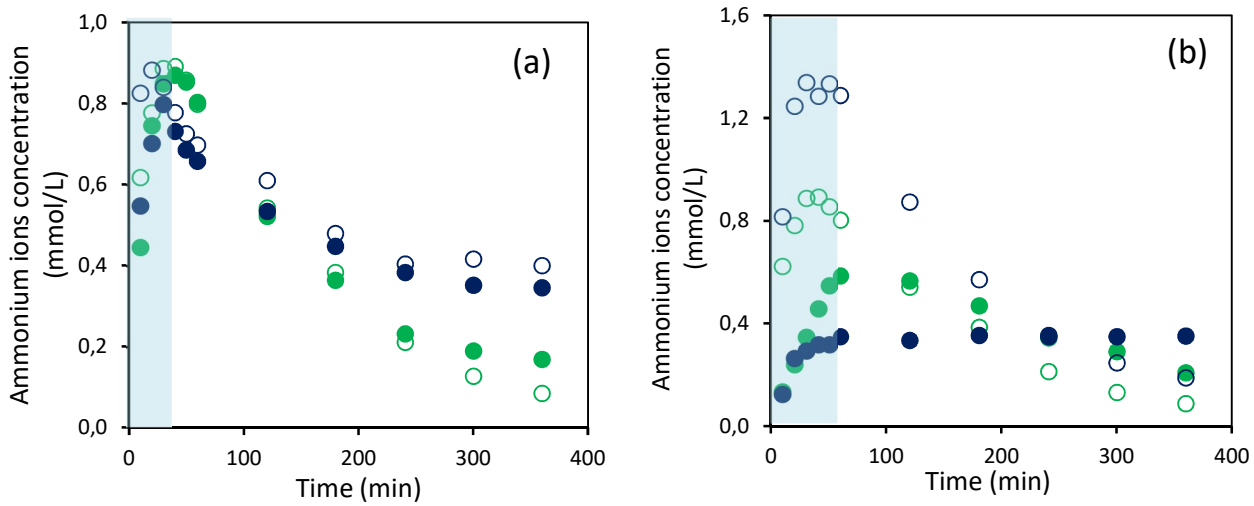

Fig. 11. Influence of the palladium loading and reduction temperature on the concentration profiles of ammonium ions vs. time formed during the reduction of nitrites by hydrogen in batch conditions : (a) on Pd/CZ(EISA) and (b) Pd/CZ(COP) – full symbol reduction at 300°C, open symbol reduction at 500°C – 0.46 wt%Pd in blue and 2.3 wt.% Pd in green.

Table 3. Initial rate measurements performed at 20°C on Pd/$Ce_{0.5}Zr_{0.5}O_2$ (0.46Pd/CZ and 2.3Pd/CZ) during the reduction of nitrite to nitrogen.

Catalyst	$T_{Red.}$ (°C)	d_{Pd} (nm)	Initial rate ($mol.h^{-1}.g_{Pd}^{-1}$)	TOF (h^{-1})	Interfacial rate ($10^{-12}\mu mol.s^{-1}.cm^{-1}$)	$NH_4^{+\,a}$ at max	$NH_4^{+\,b}$ at the end
2.3Pd/CZ(EISA)	300	6.1	5.0×10^{-2}	29.3	8.4	15.8	3.0
2.3Pd/CZ(COP)	300	10.9	4.6×10^{-2}	47.6	24.2	10.5	3.5
0.46Pd/CZ(EISA)	300	8.6	11.6×10^{-2}	95.2	38.2	14.2	6.2
0.46Pd/CZ(COP)	300	10.2	1.9×10^{-2}	33.8	30.3	6.1	6.3
2.3Pd/CZ(EISA)	500	19.9	3.4×10^{-2}	64.4	75.1	16.0	1.7
2.3Pd/CZ(COP)	500	49.3	3.7×10^{-2}	175.9	499	16.0	1.7
0.46Pd/CZ(EISA)	500	31.7	15.8×10^{-2}	474.6	886	15.4	7.0
0.46Pd/CZ(COP)	500	30.1	2.6×10^{-2}	74.0	130	24.0	3.3

[a] Ammonia concentration formed at maximum expressed in mg/L
[b] Residual ammonia concentration formed at the end of the reaction expressed in mg/L

4. Discussion

This study clearly demonstrates the complexity for optimizing the surface properties by combining reducible support materials and palladium particles. Indeed, previous investigations shown that catalytic improvements in the reduction of nitrates can be obtained by combining a reducible materials and the zero-valent states of precious metals [14]. However, this statement is

purely qualitative. At a first glance, this concept could be widened in the reduction of nitrites since the formation of anionic vacancies could facilitate the adsorption of nitrites and metallic sites would be supposed to activate the dissociation of hydrogen. Subsequent, diffusion of dissociated hydrogen species at the metal-support interface would finally reduce adsorbed nitrites. However, particular attention should be paid to the nature of the crystal phase which can influence oxygen mobility and the ease to create anionic vacancies. Indeed, $Ce_xZr_{1-x}O_2$ mixed oxides with high zirconium content, stabilizing a tetragonal structure, could have detrimental effects by suppressing the anionic mobility [64]. Moreover, in some extent the kinetic behavior of nano-sized metallic Pd particles can be governed by structural requirements since the reduction on nitrites is recognized structure sensitive [62] or particle size dependent [61,65]. Generally speaking, the isolation of these two parameters is never an easy task and could be somewhat conflicting.

As demonstrated in this study, the implementation of different methods for the preparation of $Ce_{0.5}Zr_{0.5}O_2$ can lead to solids exhibiting different bulk and surface properties which can potentially influence the nature and the extent of interactions with palladium. In terms of structural properties, the Evaporation Induced Self-Assembly method leads mainly to the stabilization of the tetragonal structure for ceria-zirconia mixed oxides with no detectable inhomogeneity in bulk composition. Importantly, bare and Pd-doped $Ce_{0.5}Zr_{0.5}O_2$ samples prepared according to the EISA procedure exhibit significant surface zirconium enrichment. In contrast, the solids prepared by co-precipitation are surface cerium enriched samples which can be simply explained by a partial segregation of CeO_2 proven by Raman spectroscopy with a sharp intensification of the 490 cm^{-1} Raman band related to the preferential growth of a cubic fluorite structure. These observations are consistent with different textural properties with the formation of a broad bimodal pore size distribution emphasizing the coexistence of different segregated phases on Pd/CZ(COP), i.e., the cubic structure of CeO_2 coexisting with the tetragonal structure of ceria-zirconia mixed oxide. Those different structural and textural features also coincide with different behavior in terms of reducibility with reduction processes taking place more readily at the surface of the segregated CeO_2 phase characterizing Pd/CZ(COP) samples. As a consequence, the estimation of higher Ce^{3+}/Ce^{4+} ratio from XPS analysis on *ex situ* reduced Pd/CZ(COP) would be consistent with a higher density of anionic vacancies with expected beneficial effects in terms of catalytic properties compared to the series prepared by the

EISA method. XPS measurements also provide important information with respect to the oxidation state of palladium related to the observation of metallic Pd species on the series prepared by coprecipitation. In agreement with Kim et al. [19], the promotion of stronger metal-support interactions on Pd/CZ(COP) could stabilize electron-rich palladium particles. Hence, on the basis of the statement postulated by Kim et al. [14] one can predict that the series obtained by coprecipitation could exhibit higher catalytic performances in terms of activity if we assume the participation of metallic sites at the vicinity of anionic vacancies.

As shown, the normalized rate expressed per gram of palladium provide an overall information which undoubtedly show the superiority of 0.46Pd/CZ(EISA) reduced at the lowest temperature, i.e., 300°C, which formally is not helpful to differentiate the particle size dependency or the role played by the metal-support interface. Surprisingly the normalized rate expressed per gram of palladium measured on reduced samples at 500°C are comparable still verifying the highest performances of 0.46Pd/CZ(EISA) while at higher reduction temperature an increase of the density of anionic vacancies jointly to a greater metallic character should enhance the reaction rate [14]. XPS also reveal a greater metallic character on the reduced samples on Pd/CZ(COP) which could a priori benefit the catalytic activity.

To go a little bit further the TOF were estimated on the basis of chemisorption measurements. In addition we roughly estimated the specific rate based on the length of periphery of Pd-$Ce_xZr_{1-x}O_2$ interface as earlier described [66,67]. In fact the length of the perimeter of metallic Pd particles I_0 can be calculated by assuming hemispherical particles with a circular geometry at the interface and taking the Pd density ρ_{Pd} = 12.02 g.cm^{-3} into account. The obtained values for I_0 oscillate in the range (0.3-45.1)×10^{11} cm.g^{-1} leading to interfacial rates expressed per cm in Table 3. Previous investigations [67] found that the comparison between TOF and interfacial rates is useful to identify different kinetic regimes. Indeed, a rise in interfacial rate at constant TOF values with increasing particle size was previously observed on Pt/$LaFeO_3$ for the NO/H_2 reaction and led the authors to the conclusion that the metal-support interface would govern the kinetics. In the opposite way, the role of the Pt-$LaFeO_3$ interface was found negligible, recovering a structure sensitive reaction involving only metallic Pt atoms as active sites on specific oriented surfaces. As shown in Table 3, no decisive arguments are brought from the comparison of the TOF and interfacial rates when Pd/CZ catalysts are reduced at 300°C. Indeed the values likely vary within the margin of error and the weak particle size dependency of the

TOF correspond to a very narrow range of particle size 6-11 nm, (see Fig. 12) compared to previous investigations which demonstrated a structure-sensitivity on much larger particles [65,68]. In fact, significant differences arise when the catalysts are reduced at 500°C. As seen in Table 3, the range of particle sizes d_{Pd} widens up to 50 nm, in parallel, the surface is likely more reduced corresponding to a greater density of anionic vacancies. As a result, a sharp increase of the TOF and interfacial rates on Pd/CZ is observable but in the same extent which is unable to discriminate between the structure sensitivity and the prevalence of the metal-support interface on the kinetics. On the other hand, this comparison accentuates the peculiar properties of 0.46Pd/CZ(EISA).

As previously shown on precious metal catalysts supported on reducible titania, strong-metal support interactions induce electron-rich active metal state via the formation of partially reduced TiO_{2-x} aggregates which can influence both the rate and the selectivity. Interestingly, a careful monitoring of the electron density on Pt/CeO_2 was found to avoid an over production of ammonia [20]. In practice, the initial rate of production of ammonia shown in Fig. 11 is in rather good agreement with the maximum concentration reported in Table 3 which emphasizes the fact that the production of ammonia seems to occur more readily on samples reduced at 500°C. Accordingly, the subsequent comparison between 0.46Pd/CZ(EISA) and 0.46Pd/CZ(COP) seems to be relevant with maxima in ammonium concentration of respectively 15.4 and 24.0 mg/L. In agreement with previous statements, such difference could suggest different extent in electron transfer especially if Pd interacts differently with the tetragonal ceria-zirconia solid solution and with CeO_2 on Pd/CZ(COP). In this latter case a more extensive electron donation could explain a sharp increase in ammonia formation. This explanation seems consistent with a greater stabilization of metallic Pd species on Pd/CZ(COP) reduced at 300°C as evidenced from XPS analysis. Alternately, a specific morphology of Pd particles with preferential orientated surfaces due to different interactions with reduced CeO_2 instead of $Ce_xZr_{1-x}O_2$ solid solution could be a key parameter in monitoring the rate and the selectivity of the reaction in favor of nitrogen or ammonia. This statement has been earlier put in evidence on Pt supported on $LaFeO_3$ with epitaxial growth of Pt particles with preferential (111) surface [67]. Although, no decisive conclusion in this study regarding the nanostructure of such systems would need more exhaustive advanced characterization, our results seems to be more in favor of the explanation given by Epron et al. [59] showing that the reduction of nitrites would predominantly take place

on Pt particles on CeO_2 whereas the redox properties of the support would be preferentially involved in the reduction of nitrates to nitrites. Based on this, the changes observed on the rates and the selectivities recorded on on Pd/CZ(COP) and Pd/CZ(EISA) could be more rationalized in terms of strength of metal-support interaction depending on the presence of inhomogeinity modifying the electron density of palladium particles.

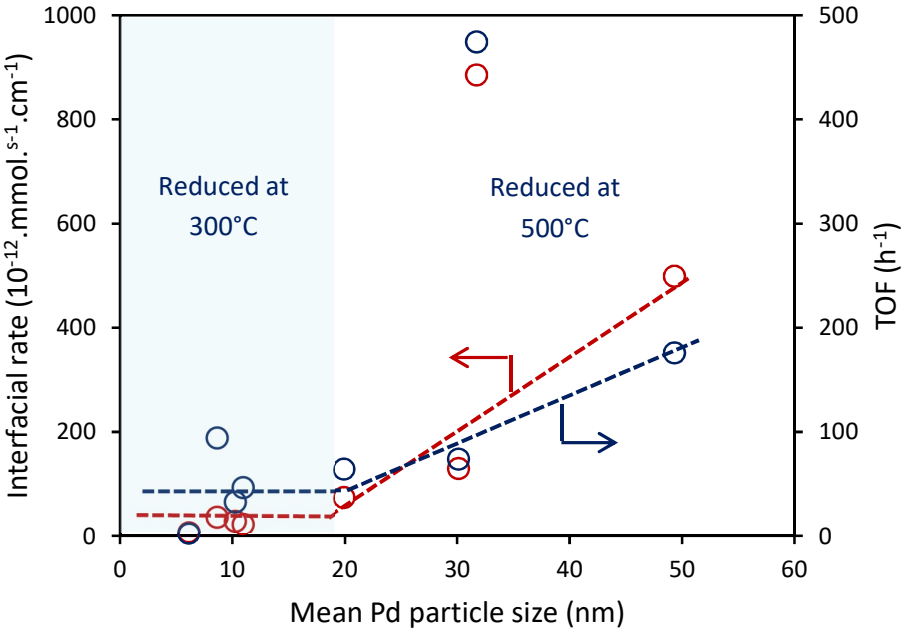

Fig. 12. Comparison of TOF and interfacial rates vs. mean Pd particle size on Pd/CZ

5. Conclusion

This study reports the influence of the support materials on the catalytic properties of Pd particles in the reduction of nitrites in aqueous phase performed at 20°C. Ceria-zirconia mixed oxide ($Ce_{0.5}Zr_{0.5}O_2$) as support was prepared according to co-precipitation and evaporation-induced self-assembly methods and then calcined in air at 400°C. Straightforward bulk and surface characterizations showed a preferential tetragonal structure for the mixed-oxide prepared from the EISA method exhibiting a surface zirconium enrichment whereas the co-precipitation method leads to strong inhomogeneity in composition with the segregation of the fluorite

structure of CeO_2 coexisting with the mixed oxide. As a consequence some significant deviations are observed on the surface composition with surface cerium enrichment corresponding to a greater formation of anionic vacancies reflected by higher Ce^{3+}/Ce^{4+} ratio on sample reduced at 300°C. Such structural changes have also some consequence on the textural properties with monomodal pores size distribution on CZ(EIZA) whereas the CZ(COP) is characterized by a bimodal distribution with larger pores likely associated to the formation of CeO_2. All those changes can alter the impregnation of palladium which was found more poorly dispersed on CZ(COP) irrespective of the reduction temperature, i.e., 300°C or 500°C under pure hydrogen.
Catalytic measurements show a faster reduction of nitrates on samples reduced at 500°C with a prominent production of ammonia at the early stage of the reaction at the expense of nitrogen the target molecule. Unprecedented selectivity behavior is observed with a sequential ammonia consumption promoted on $Pd/Ce_{0.5}Zr_{0.5}O_2$ irrespective of the preparation route. The changes observed in the reaction rates are strongly dependent on the pre-reduction leading to significant enhancements when the pre-reduction is performed at 500°C. The comparison of TOF and interfacial rates expressed per cm, reflecting the length of the perimeter of metallic Pd particles, versus the particle size does not provide clear evidence to privilege the prevalence of structural or electronic factors which could govern the catalytic properties but highlight the superiority of 0.46Pd/CZ(EISA) compared to all other samples. However, it seems that there is no strong evidence that the support materials would directly participate to the reaction especially on the EISA support stabilizing a tetragonal structure known for exhibiting lower redox properties than the cubic form. This seems in relative good agreement with previous investigation that showed nitrite reduction would occur through classical mechanism involving only metallic sites, the involvement of oxygen vacancies being more obvious for the reduction of nitrates to nitrites.

Acknowlegments

The authors greatly acknowledge the financial support from the CCIFER – ANCS and the French Embassy (PhD fellowship awarded to S. Troncéa who won the competition *« Graine de Chercheur et Energie Durable »*). Chevreul Institute (FR 2638), Ministère de l'Enseignement Supérieur et de la Recherche, Région Nord – Pas de Calais and FEDER are acknowledged for

supporting and funding partially this work. Sandra Casale (UPMC, Paris VII) is acknowledged for conducting SEM measurements.

Reference

1. L.J. Puckert, Environ. Sci. Technol. 29 (1995) 408A-414A.
2. U.S. Environmental Protection Agency (USEPA) (2008) Title 40, Part 141.54:425.
3. K. Reddy, Water Res. 34 (2000) 995-1001
4. M. Al Bahri, L. Calvo, M.A. Gilarranz, J.J. Rodriguez, F. Epron, Appl. Catal. B 138–139. (2013) 141–148.
5. F. Epron, F. Gauthard, C. Pineda, J. Barbier, J. Catal. 198 (2001) 309–318.
6. Y.N. Kim, M.Y. Kim, M. Choi, Chem. Eng. J. 289 (2016) 423-432.
7. D.P. Durkin T. Ye, J. Choi, K.J.T. Livi, H.C. De Long, P.C. Turlove, D.H. Fairbrother, L.M. Haverhals, D. Shuai, Appl. Catal. B 221 (2018) 290-301.
8. S. Hörold, K.D. Vorlo, T. Tacke, M. Sell, Catal. Today, 17 (1993) 21–30.
9. A. Suda, H. Sobukawa, T. Suzuki, T. Kandori, Y. Ukyo, M. Sugiura J. Ceram. Soc. Jpn 109 (2001) 177–180.
10. S. Letichevsky, C.A. Tellez, R.R. de Avillez, M.I.P. da Silva, M.A. Fraga MA, L.G. Appel, Appl. Catal B: Environ. 58 (2005) 203–210.
11. A.I. Kozlov, D.H. Kim, A. Yezerets, P. Andersen, H.H. Kung, M.C. Kung J. Catal. 209 (2002) 417–426.
12. A. Pintar, J. Batista, J. Levec, T. Kajuchi, Appl. Catal. B 11 (1996) 81–98.
13. Y. Yoshinaga, T. Akita, I. Mikami, T. Okuhara, J. Catal. 207 (2002) 37–45.
14. M.-S. Kim, D.-W. Lee, S.H. Chung, J.T. Kim, I.-H. Cho, K.-Y. Lee, J. Mol. Catal. A 392 (2014) 308–314.
15. J. Kugai, J.T. Miller, N. Guo, C. Song, Appl. Catal B: Environ. 105 (2011) 306–316.
16. X. Huo, D.J. Van Hoomissen, J. Liu, S. Vyas, Appl. Catal. 211 (2017) 188-198.
17. A.H. Pizarro, C.B. Molina, J.J. Rodriguez, F. Epron, J. Env. Chem. Eng. 3 (2015) 2777-2785.
18. J.K. Chinthaginjala and L. Lefferts, Appl. Catal. B. 101 (2010) 144-149.
19. M.-S. Kim, S.-H. Chung, C.J. Yoo, M.S. Lee, I.-H. Cho, D.-W. Lee, K.-Y. Lee, Appl. Catal. B 142–143 (2013) 354–361.
20. N. Barrabés, A. Dafinov, F. Medina, J.E. Sueiras, Catal. Today 149 (2010) 341–347
21. E.L. Crepaldi, G. J. D. A. Soler-Illia, A. Bouchara, D. Grosso, D. Durand, C. Sanchez, Angew. Chem. Int. Ed. 42 (2003) 347–351.
22. Q. Yuang, Q. Liu, W.G. Song, W. Feng, W.L. Pu, L.D. Sun, Y.W. Zhang, C.H. Yan, J. Am. Chem. Soc. 2007, 129, 6698-6699.
23. M.A. Ebiad,Dalia R. Abd El-Hafiz, R.A. Elsalamony, L.S. Mohamed, RSC Adv. 2 (2012) 8145–8156.
24. S. Salasc, V. Perrichon, M. Primet, N. Mouaddib-Moral, J. Catal. 206 (2002) 82–90.
25. R. Di Monte, J. Kaspar, P. Fornasiero, A. Ferrero, G. Gubitosa, M. Graziani, Stud. Surf. Sci. Catal. 116 (1998) 559–569.
26. L. Xu, H. Song, L. Chou, Int. J. Hyd. En. 37 (2012) 18001–18020.
27. F. Zhang, C.H. Chen, J.C. Hanson, R.D. Robinson, I.P. Herman, S.W. Chan, J. Am. Ceram. Soc. 89 (2006) 1028–1036.
28. M. Li, Z. Feng, G. Xiong, P. Ying, Q. Xin, C. Li, J. Phys. Chem B 105 (2001) 8107–8111.

29. J. Serrano-Ruiz, J. Luettich, A. Sepúlveda-Escribano, F. Rodríguez-Reinoso, J. Catal. 241 (2006) 45–55.
30. C. Tiseanu, V.I. Parvulescu, D. Avram, B. Cojocaru, M. Boutonnet, M. Sanchez-Dominiguez, Phys. Chem. Chem. Phys., 2014, 16, 703–710.
31. I. Atribak, B. Azambre, A. Bueno López, A. García-García, Appl. Catal. B 92 (2009) 126–137.
32. W. Mista, T. Rayment, J. Hanuza, L. Macalik, Mater. Sci. Poland 22 (2004) 153–170.
33. B. Zhao, Q.Y. Wang, G.F. Li, R.X. Zhou, J. Alloys Comp. 508 (2010) 500–506.
34. B.M. Reddy, P. Bharali, P. Saikia, S.-E. Park, M.W. van den Berg, M. Muhler, W. Grünert, J. Phys. Chem. C 112 (2008) 11729-11737.
35. M. Yashima, H. Arashi, M. Kakihana and M. Yoshimura, J. Am. Ceram. Soc. 77 (1994) 1869–1874.
36. F.B. Passos, E.R. de Oliveira, L.V. Mattos, F.B. Noronha, Catal. Today 101 (2005) 23-30.
37. P. Fornasiero, G. Balducci, R. Di Monte, J. Kaspãr, V. Sergo, G. Gubitosa, A. Ferrero, M. Graziani, J. Catal. 164 (1996) 173–183.
38. M. Teng, L. Luo, X. Yan, Micr. Meso. Mater. 119 (2009) 158–164.
39. N.S. Priya, C. Somayaji, S. Kanagaraj, Proc. Eng. 64 (2013) 1235-1241.
40. A. Trovarelli, J. Inorg. Chem. 20 (1999) 263–284.
41. L. Xu, H. Song, L. Chou Int. J. Hydr. En. 37 (2012) 18001–18020.
42. J. Kaspar, P. Fornasiero, M. Graziani, Catal. Today 50 (1999) 285–298.
43. C. Bozo, N. Guilhaume, E. Garbowski, M. Primet, Catal. Today, 59 (2000) 33–45.
44. P. Fornasiero, J. Kaspar, M. Graziani, J. Catal. 167 (1997) 576–580.
45. B. Zhao, G.F. Li, C.H. Ge, Q.Y. Wang, R.X. Zhoua, Appl. Catal. B 96 (2010) 338–349.
46. H. Muraki, K. Yokota and Y. Fujitani, Appl. CataI., 48 (1989) 93–105.
47. G. Chen, W-T. Chou and C-T. Yeh, Appl. Catal., 8 (1983) 389–397.
48. I. Halasz, A. Brenner, M. Shelef, K.Y.S. Ng, Appl. Catal. A 82 (1992) 51-63.
49. F. Le Normand, J. El Fallah, L. Hilaire, P. Légaré, A. Kotani, J.C. Parlebas, Solid State Comm. 71(11) (1989) 885–889.
50. M. Brun, A. Berthet, J.C. Bertolini J. Electron Spectrosc. Relat. Phenom. 104 (1999) 55–60.
51. D. Briggs, M.P. Seah, In Practical Surface Analysis (2nd Ed.), Vol.1, John Wiley: Chichester, 1999, p. 599.
52. W. Huang, Z. Zuo, P. Han, Z. Li, T. zhao, J. Electron Spectrosc. Relat. Phenom. 173 (2009) 88–95.
53. E.M. Slavinskaya, O.A. Stonkus, R.V. Gulyaev, A.S. Ivanova, V.I. Zaikovskii, P.A. Kuznetsov, A.I. Boronin, Appl. Catal. A 401 (2011) 83–97.
54. K. Otto, L.P. Haack, J.E. de Vries, Appl. Catal. B 1 (1992) 1–12.
55. M. Moroseac, T Skála, K. Veltruská, V. Matolín, I. Matolínová, Surf. Sci. 56 (2004) 1118–1123.
56 X. Huo, D.J. Van Hoomissen, J. Liu, S. Vyas, Appl. Catal. 211 (2017) 188-198.
57. A.H. Pizarro, C.B. Molina, J.J. Rodriguez, F. Epron, J. Env. Chem. Eng. 3 (2015) 2777-2785.
58. J.K. Chinthaginjala and L. Lefferts, Appl. Catal. B. 101 (2010) 144-149.
59. F. Epron, F. Gauthard, J. Barbier, J. Catal. 206 (2002) 363–367.
60. J. Lee, Y.G. Hur, M.-S. Kim, K.-Y. Lee, J. Mol. Catal. A 399 (2015) 48–52.
61. F. Zhang, S. Miao, Y. Yang, X. Zhang, J. Chen, N. Guan, J. Phys. Chem. C 112 (2008) 7665–7671.
62. Y. Yoshinaga, T. Akita, I. Mikami, T. Okuhara, J. Catal. 207 (2002) 37–45.
63. B. Ileri, O. Ayyildiz, O. Apaydin, J. Hazardous Mater. 292 (2015) 1–8.
64. S.A. Ghom, C.Z. Zamani, S. Nazarpour, T. Andreu, J.R. Morante, Sensors and Act. B 140 (2009) 216–221.
65. J.K. Chinthaginjala, A. Villa, D.S. Su, B.L. Mojet, L. Lefferts, Catal. Today 183 (2012) 119–123.
66. C.M. Kalamaras, S. Americanou, A.M. Efstathiou, J. Catal. 279 (2011) 287–300.
67. Y. Wu, C. Dujardin, C. Lancelot, J.P. Dacquin, V.I. Parvulescu, M. Cabié, C.R. Henry, T. Neisius, P. Granger, J. Catal. 328 (2015) 236–247.
68. A. Miyazaki, T. Asakawa, Y. Nakano, I. Balint, Chem. Commun. (2005) 3730–3732.